

# <sup>1</sup> Beam Position Reconstruction for the g2p Experiment <sup>2</sup> in Hall A at Jefferson Lab

<sup>3</sup> Pengjia Zhu<sup>a,\*</sup>, Kalyan Allada<sup>b,g</sup>, Trent Allison<sup>b</sup>, Toby Badman<sup>c</sup>, Alexandre  
<sup>4</sup> Camsonne<sup>b</sup>, Jian-ping Chen<sup>b</sup>, Melissa Cummings<sup>d</sup>, Chao Gu<sup>e</sup>, Min Huang<sup>f</sup>,  
<sup>5</sup> Jie Liu<sup>e</sup>, John Musson<sup>b</sup>, Karl Slifer<sup>c</sup>, Vincent Sulkosky<sup>e,g</sup>, Yunxiu Ye<sup>a</sup>, Jixie  
<sup>6</sup> Zhang<sup>b,e</sup>, Ryan Zielinski<sup>c</sup>

<sup>a</sup>University of Science and Technology of China, Hefei, Anhui 230026, China

<sup>b</sup> Thomas Jefferson National Accelerator Facility, Newport News, VA 23606, USA

<sup>9</sup> <sup>c</sup> University of New Hampshire, Durham, NH 03824, USA  
<sup>b</sup> The University of Texas at Austin, TX 78712, USA

<sup>10</sup> <sup>d</sup>College of William & Mary, Williamsburg, VA 23187, USA  
<sup>e</sup>University of Virginia, Charlottesville, VA 22904, USA

<sup>11</sup> *e University of Virginia, Charlottesville, VA 22904, USA*  
*f Duke University, Durham, NC 27710, USA*

<sup>12</sup>*Duke University, Durham, NC 27708, USA*  
<sup>13</sup>*Massachusetts Institute of Technology, MA 02139, USA*

<sup>13</sup> Massachusetts Institute of Technology, MA, 02139, USA

14 Abstract

Beam-line equipment was upgraded for experiment E08-027 (g2p) in Hall A at Jefferson Lab. Two beam position monitors (BPMs) were necessary to measure the beam position and angle at the target. A new BPM receiver was designed and built to handle the low beam currents (50-100 nA) used for this experiment. Two new super-harps were installed for calibrating the BPMs. In addition to the existing fast raster system, a slow raster system was installed. Before and during the experiment, these new devices were tested and debugged, and their performance was also evaluated. In order to achieve the required accuracy (1-2 mm in position and 1-2 mrad in angle at the target location), new methods were developed for analyzing the data of the BPMs and harps, as well as reconstructing the beam position and angle event by event at the target location. The calculated beam position will be used in the data analysis to accurately determine the kinematics for each event.

<sup>15</sup> *Keywords:* g2p; BPM; raster; beam position

\*Corresponding author

*Email address:* pzhujlab.org, zhupj55@mail.ustc.edu.cn (Pengjia Zhu)

16     **1. Introduction**

17     A polarized ammonia ( $NH_3$ ) target was used for the first time in Hall A for  
18     the g2p experiment [1]. It operated at a low temperature of 1K and a strong  
19     transverse magnetic field of either 5 T or 2.5 T. A high electron beam current  
20     would cause significant target polarization drop due to target temperature rising  
21     and ionization radiation to the target material [2]. To minimize depolarization,  
22     the beam current was limited to below 100 nA and a raster system was used  
23     to spread the beam spot out to a larger area. The transverse magnetic field  
24     in the target region would cause the beam to be deflected downward when the  
25     beam enters the target region. To compensate for this, two chicane magnets  
26     were placed in front of the target to pre-bend the beam upwards. Due to the  
27     low beam current and tight space limitations after the chicane magnets, the  
28     experimental accuracy goals for the position (1-2 mm) and angle (1-2 mrad) at  
29     the target were challenging to achieve. New beam-line devices and an associated  
30     readout electronics system were designed for the g2p experiment to accomplish  
31     these goals. Design details and the performance of the beam-line devices will  
32     be described in the following sections along with a discussion of a new analysis  
method determine the beam position and direction.

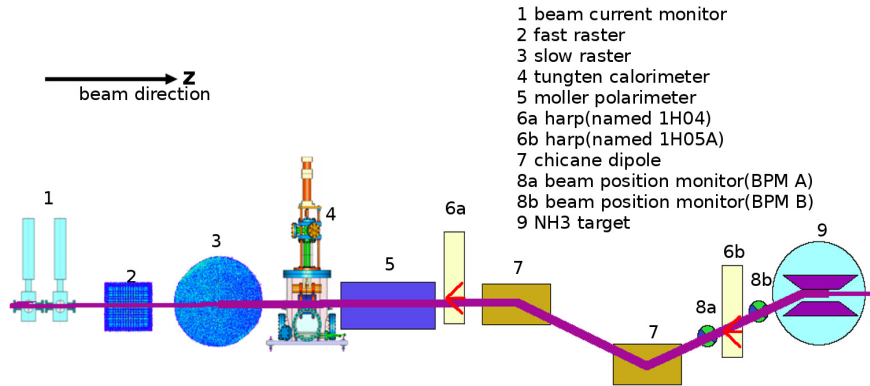


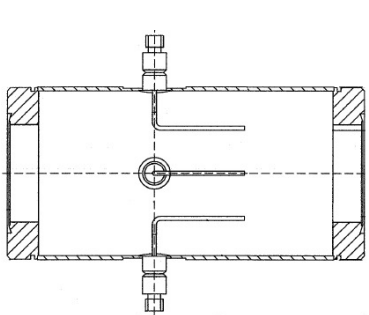
Figure 1: Schematic of beamline components for g2p experiment

34    **2. Beam-line Instrumentation**

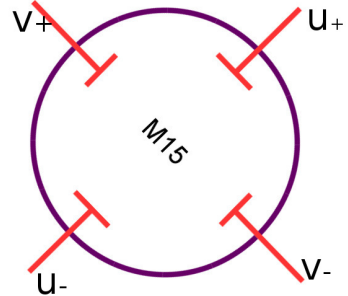
35    *2.1. Beam position monitor (BPM)*

36    The scattering angle of the outgoing lepton in deep inelastic scattering, which  
37    is defined with respect to the direction of the incident beam, is an important  
38    variable for obtaining meaningful physics results. Therefore, the position and  
39    direction of the beam, after being bent by the chicane magnetic field and spread  
40    out by the rasters, must be measured precisely. Two BPMs and two harps were  
41    installed for relative and absolute measurements of beam position and direction  
42    near the target, respectively.

43    The BPM consists of four open-ended antennas for detecting the beam po-  
44    sition; the measurement is non-invasive to the beam. The BPM chambers  
45    shown in Fig.2 are part of the beam pipe. The four antennas are attached  
to feedthroughs on the interior wall of the pipe at  $90^\circ$  intervals. The BPM



(a) BPM design diagram, from JLab in-  
strumentation group



(b) BPM chamber which contains 4 an-  
tennas

Figure 2: BPM chamber

46  
47    chambers are placed with a  $45^\circ$  rotation (along z) with respect to the global  
48    Hall coordinate. The two pairs of antennas are marked as  $u_+$ ,  $u_-$  and  $v_+$ ,  $v_-$ ,  
49    respectively, which are used to determine beam positions in  $u$  and  $v$  directions.  
50    When the beam passes through the BPM chamber, each antenna receives an  
51    induced signal. The BPM front-end receiver collects and sends the signal to

52 the regular Hall A DAQ system and another DAQ system designed for parity  
53 violation experiments, the HAPPEX system [3]. The new BPM receiver was  
54 designed by the JLab instrumentation group [4] in order to achieve the required  
55 precision at a level of 0.1 mm with a beam current as low as 50 nA. The regular  
56 DAQ system was connected to a 13-bit fastbus ADC (Lecroy ADC 1881) with  
57 an integration time of 50 ns, which was triggered by a scattered electron event.  
58 The HAPPEX system was connected to an 18-bit ADC with an integration  
59 time of 875  $\mu$ s, which was triggered by a beam helicity signal at 1 kHz. The  
60 amplitude,  $A$ , recorded in the ADC has the following relation with the BPM  
61 signal,  $\phi$ :

$$A \propto \phi \cdot 10^{g/20}, \quad (1)$$

62 where  $g$  is the gain of the receiver.

63 The BPM receiver generates a large time delay for the output signals. The  
64 digital filter used in the receiver contributes 1/175 s delay time, which was the  
65 inverse of the bandwidth setting chosen for the filter. There is a  $\sim 4 \mu$ s delay  
66 as a result of finite processing times. The BPM can not provide event by event  
67 position because of this time delay, due to the 25 kHz fast raster system.

68 Because of the space limitation between the second chicane magnet and the  
69 target, the two BPMs were placed close to each other. One was placed 95.5 cm  
70 upstream of the target while the other was placed 69 cm upstream, making the  
71 distance between them only 26.5 cm. The short distance magnified the position  
72 uncertainty from the BPMs to target.

73 *2.2. Super harp*

74 Two super harps were designed and installed in the beam-line, as shown in  
75 Fig.1 (label 6a - 1H04 and 6b - 1H05A), to provide an absolute measurement  
76 of the beam position for calibration of the BPMs. The new harps were able to  
77 work in pulsed beam (1% duty factor) with a current of several  $\mu$ A. A diagram  
78 for the harp is shown in Fig.3,

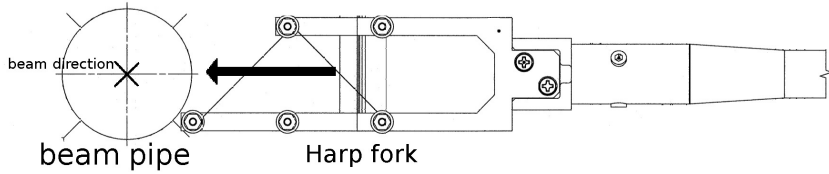


Figure 3: Harp diagram

79 which consists of three wires with a thickness of  $50 \mu\text{m}$ , a fork and a controller  
 80 chassis. The harp chamber is perpendicular to the beam pipe and connected  
 81 to the beam pipe as part of the vacuum chamber of the beamline. The two  
 82 harps have different configurations of three wires: vertical(|), bank left(\), and  
 83 bank right(/) for 1H04, and /, |, \ for 1H05. The angle of the / or \ wires is  
 84  $45^\circ$  relative to the wire dock frame. The wires are arranged in a fork (Fig.3)  
 85 controlled by a step motor [5] which can be moved in and out of the beam-line.  
 86 The harps must be moved out of the beam-line when production data is being  
 87 taken because they are invasive to the beam. The original position of the wires  
 88 was surveyed before the experiment at a precision level of  $0.1 \text{ mm}$ . As the motor  
 89 driver moved the fork through the beam, each wire received a signal, which was  
 90 recorded for further analysis. The signals received from the wire and the step-  
 91 counters from the motor driver were then sent to an amplifier and the DAQ.  
 92 The amplification and the speed of the motor were adjustable for the purpose  
 93 of optimizing the signals of each scan. Recorded data combined with the survey  
 94 data was used to calculate the absolute beam position.

95 The signal from the | wire ( $\text{peak}_{|}$ ) was used for getting the  $x$  position ( $x_{\text{harp}}$ )  
 96 of the beam , and the signals from the /, \ wires ( $\text{peak}_{/}$  and  $\text{peak}_{\backslash}$ ) were used  
 97 for getting the  $y$  position ( $y_{\text{harp}}$ ):

$$\begin{aligned}
 x_{\text{harp}} &= \text{survey}_{|} - \text{peak}_{|} \\
 y_{\text{harp}} &= \frac{1}{2}[(\text{survey}_{\backslash} - \text{survey}_{/}) - (\text{peak}_{\backslash} - \text{peak}_{/})]
 \end{aligned} \tag{2}$$

98      *2.3. Raster system*

99      In order to minimize the depolarization, avoid damage to the target material  
100     from radiation, and reduce systematic error for the polarization measurement  
101     by NMR (The polarization of the  $NH_3$  target was measured using a NMR coil  
102     which was placed inside the target cell [6]. The non-uniformity of depolarization  
103     could reduce the precision of the NMR measurement due to the measurement  
104     being an average over the target), two raster systems were installed at  $\sim 17$  m  
105     upstream of the target, as shown in Fig.1 (labels 2 and 3 for fast and slow rasters,  
106     respectively). Both the fast and slow rasters consist of two dipole magnets. The  
107     same triangular waveforms with frequency of 25 kHz were used to drive the  
108     magnet coils of the fast raster to move the beam in x and y directions, forming  
109     a rectangular pattern of  $2\text{ mm} \times 2\text{ mm}$ , as shown in Fig.4.

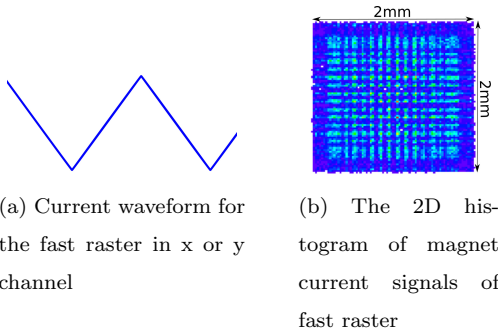


Figure 4: Fast raster pattern

109  
110     A dual-channel function-generator<sup>1</sup> was used to generate two independent  
111     waveforms to drive the magnet coils of the slow raster. The waveforms for the  
112      $x$  and  $y$  directions are:

$$x = A_x t^{1/2} \sin(\omega t),$$

---

<sup>1</sup>agilent 33522A function generator, <http://www.home.agilent.com/en/pd-1871286-pn-33522A/function-arbitrary-waveform-generator-30-mhz>

$$y = A_y(t + t_0)^{1/2} \sin(\omega t + \phi), \quad (3)$$

113 where the  $A_x$  and  $A_y$  are the maximum amplitude,  $t_0$  and  $\phi$  are the AM and  
 sin phase difference between  $x$  and  $y$  waveform, respectively. Both of them

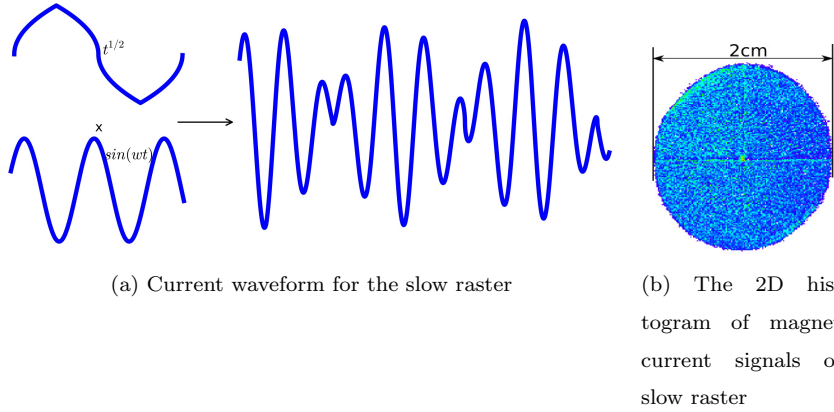
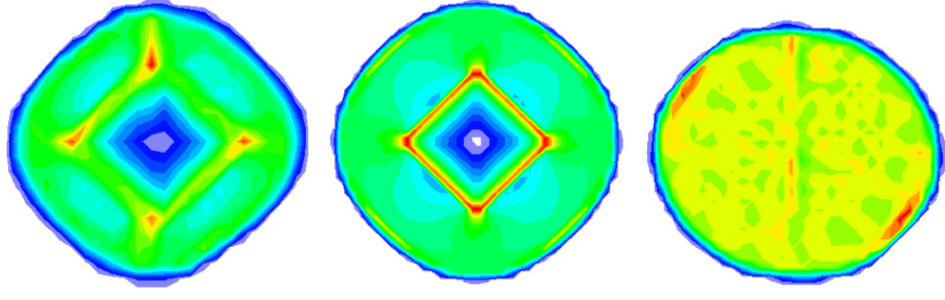


Figure 5: Slow raster pattern

114  
 115 are sine functions modulated by a function  $t^{1/2}$  in order to generate a uniform  
 116 circular pattern [7], as shown in Fig.5. The frequency of the  $x$  and  $y$  waveforms  
 117 kept same:  $\omega = 99.412$  Hz. In order to cycle the amplitude modulation (AM)  
 118 function, four piece-wise functions are combined together. The first term is  $t^{1/2}$ ,  
 119 and the second term is  $period - t^{1/2}$ , and so on for the third and fourth terms.  
 120 The cycled function has the frequency of 30 Hz.

121 The  $\phi$  was locked to  $\frac{\pi}{2}$  by the function generator, while the  $t_0$  was manually  
 122 fixed to 0. Non-zero  $t_0$  could cause a non-uniformity pattern, as shown in  
 123 Fig.6(a), which would cause non-uniformity beam distribution. A simulation  
 124 was reproduced the non-uniformity by setting the  $t_0$  to non-zero, as shown  
 125 in Fig.6(b). The  $t_0$  was carefully adjusted and minimized before production  
 126 data taking to avoid the non-uniformity. The pattern of the spread beam was  
 127 relatively uniform after this adjustment during the experiment, as shown in  
 128 Fig.6(c).



(a) Raster pattern with  $t_0 \neq 0$  (b) Simulated raster pattern, (c) Manually adjust  $t_0$  to 0 with  $t_0 \neq 0$

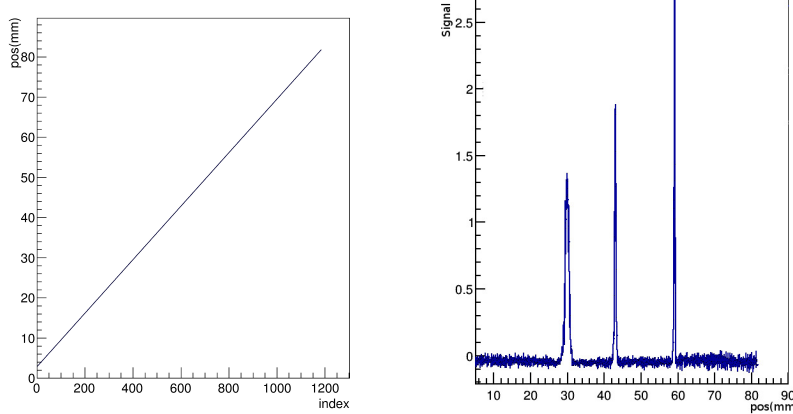
Figure 6: None-zero  $t_0$  caused slow raster non-uniformity, (a) and (c) are from the data, (b) is simulated.

**129 3. Data analysis**

**130 3.1. Harp scans for measuring absolute beam position**

**131** An example of a harp scan result is shown in Fig.7. There are three groups of  
**132** recorded data for each harp scan, which are “index”, “position”, and “signal”.  
**133** The index is related to the moving steps of the fork during the scan. Each  
**134** step of the index increases by 0.008-0.07 mm depending on the speed of the  
**135** motor driver [5]. The position is the wire location for each index. The testing  
**136** results show a good linear relation between the position and the index as shown  
**137** in Fig.7(a), because the motor speed is uniform. The line is the fitted result  
**138** with  $pos = a * index + b$ . According to this linear relation, interpolation or  
**139** extrapolation can be applied when a few data points are missing, in some cases.  
**140** The strength of signal vs. position is plotted in Fig.7(b). Each peak represents  
**141** the location when one of the three wires passed through the beam.

**142** The positions measured by the two harps were used for calibrating the beam  
**143** positions in the two BPMs. When the chicane magnets were on, beam did not  
**144** pass straight through from the first harp to the second harp. BPM calibrations  
**145** using two harps were only possible when the chicane magnets were off, i.e. in the  
**146** straight-through settings. Since the BPM was calibrated in the local coordinate



(a) position vs index for harp scan, used for extending position record

(b) Signal vs position for harp,  $x$  axis is position,  $y$  axis is the strength of signal, which is the ADC value.

Figure 7: 1H05A harp scan data

147 system, the calibration constants were independent from the settings of other  
 148 instruments. To make sure that the calibration constants for the BPMs were  
 149 still valid during the non-straight-through settings, the settings for the BPM  
 150 receiver were kept the same as in the straight-through settings during production  
 151 running.

152 The scan data from the harps was not reliable when the current of CW beam  
 153 (100% duty factor) was lower than 100 nA due to the low signal-to-noise ratio.  
 154 The harp scans were taken in pulsed mode at a current of a few  $\mu$ A, while the  
 155 BPMs were used for production data taking in CW mode at a beam current  
 156 of 50-100 nA. For a BPM calibration run, a harp scan was done first in pulsed  
 157 mode, then a DAQ run was taken immediately to record the ADC value in CW  
 158 mode without changing the beam position. The harp scan was then taken again  
 159 in the pulsed mode to double check the beam position. The harp scan data was  
 160 discarded and the scan was taken again if the beam position changed.

161    3.2. BPM data analysis and calibration

162    The traditional difference-over-sum (diff/sum) method of calculating the  
 163 beam position has the non-linearity effect at the position far away from the  
 164 center of the beam pipe [8]. It is necessary to correct the equation of diff/sum  
 165 since we have a slow raster. With the assumption of an infinitely long chamber  
 166 and the neglecting the antenna influence on the electric field inside the chamber,  
 167 the signal from each antenna excited by the beam can be calculated via image  
 168 charge method (Fig. 8) [9, 10] :

$$\phi_i = \phi_0 I \frac{R^2 - \rho^2}{R^2 + \rho^2 - 2R\rho\cos(\theta_i - \theta_0)}, \quad (4)$$

169 where  $\phi_i$  is the signal received in the antenna, and  $i$  is  $u_+$ ,  $u_-$ ,  $v_+$  and  $v_-$ ,  
 170 respectively,  $\phi_0$  is a constant related to the geometry of the BPM-chamber and  
 171 the output resistance,  $I$  is the beam current,  $R$  is the radius of the BPM vacuum  
 172 chamber,  $\rho$  is the radial position of the beam, and  $\theta_i - \theta_0$  is the angle difference  
 173 between the antenna and the beam in the polar coordinate .

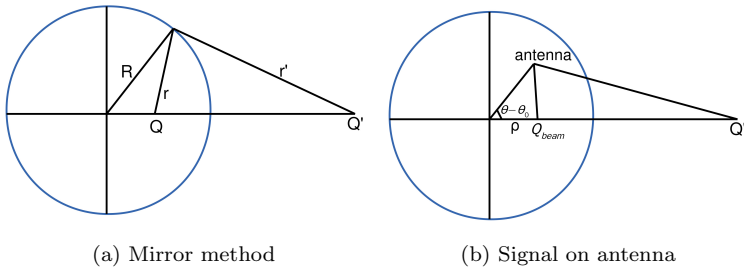


Figure 8: Signal for each antenna of BPM

173  
 174    In order to extract the beam position information, and eliminate the de-  
 175 pendence on the beam current in equation (4), the diff/sum method is used as  
 176 follows:

$$D_U = \frac{\phi_{U+} - \phi_{U-}}{\phi_{U+} + \phi_{U-}}, \quad (5)$$

177 where  $U$  is  $u$  and  $v$ , respectively. Substituting equation (4) into equation (5),  
 178 they can be rewritten as follows:

$$D_U = \frac{\phi_{U+} - \phi_{U-}}{\phi_{U+} + \phi_{U-}} = \frac{2}{R} \frac{\rho \cos(\theta - \theta_0)}{1 + \frac{\rho^2}{R^2}} = \frac{2}{R} \frac{U}{1 + \frac{\rho^2}{R^2}}, \quad (6)$$

179 where  $\rho^2 = u^2 + v^2$ . When  $u^2 + v^2 \ll R^2$ , equations (6) can be simplified as:

$$U \approx \frac{R}{2} D_U = \frac{R}{2} \frac{\phi_{U+} - \phi_{U-}}{\phi_{U+} + \phi_{U-}}. \quad (7)$$

180 Equation (7) can be used in the simple case when the beam is near the center  
 181 of the beam pipe. When the beam is far from the center, equation (7) is no  
 182 longer valid. For the g2p experiment, the beam was rastered to have a diameter  
 183 of about 2 cm at the target. From equation (6) the beam position can be  
 184 calculated as:

$$U = RD_U \left( \frac{1}{D_u^2 + D_v^2} - \frac{1}{\sqrt{D_u^2 + D_v^2}} \sqrt{\frac{1}{D_u^2 + D_v^2} - 1} \right). \quad (8)$$

185 To verify this correction equation, a simulation was performed. First, a set  
 186 of position data was generated (Fig.9(a)), and the designed radius for the BPM  
 187 chamber was used for  $R$ . Using equation (4) to get the signal for each antenna,  
 188 and setting  $\phi_0$  and  $I$  to be equal to 1, equations (8) and (7) were used to  
 189 calculate the beam position for comparison. The results are shown in Fig.9(b)  
 and 9(c), respectively.

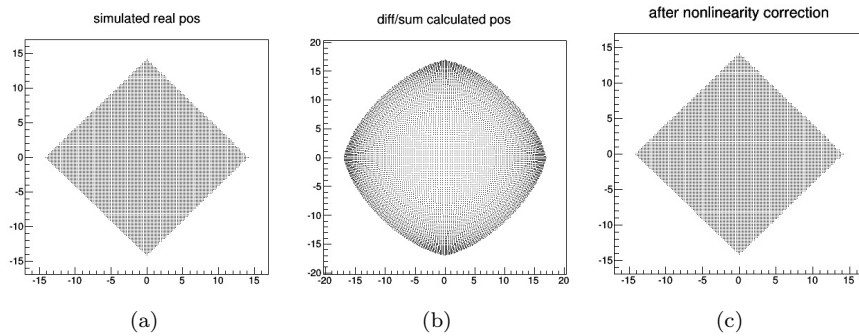


Figure 9: Comparing the calculated results using equation (7) and (8) with simulated position.  
 (a) Simulated position; (b) The calculated result with equation (7), (c) The calculated result with equation (8).

190

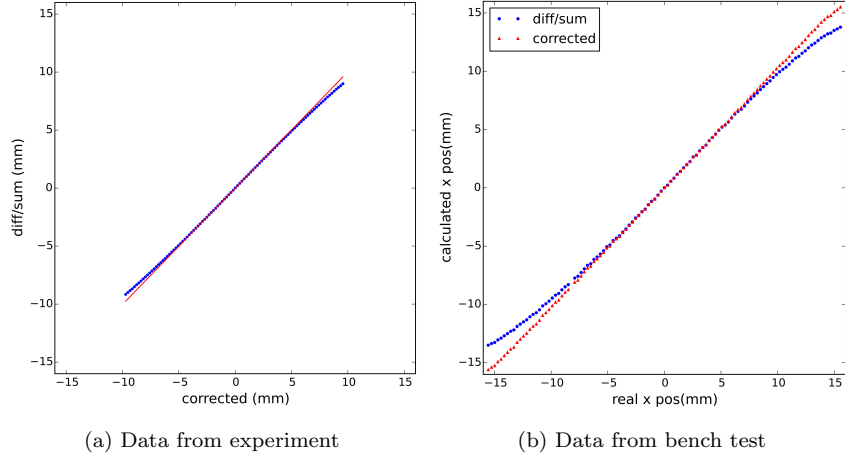


Figure 10: BPM non-linearity correction. (a) Relationship between the position calculated from diff/sum equation (6) (y axis) and the one from correction equation (8) (x axis). Red solid line is a reference line came from linear fit for the center points . Data is collected from experiment. (b) Comparison between the diff/sum equation (6) and the correction equation (8) using the bench test data. The x axis is the real beam position. The red triangles are the positions calculated from correction equation (8). The blue circles are the positions calculated from diff/sum equation (6) .

191 The correction equation is also tested by using the experiment data and the  
 192 bench test data. Fig.10(a) shows the difference between the position calculated  
 193 from the correction equation (8) and the one from the diff/sum equation (6).  
 194 Fig.10(b) shows the comparison with the real beam position from the bench test  
 195 data. In this way the method using equation (8) can correct the non-linearity  
 196 effect caused by the diff/sum method. The handling of the BPM information  
 197 which only used for the center beam position (discussed in chapter 3.4) also  
 198 reduced this non-linearity effect.

199 The final information recorded in the data-stream was designed to have a  
 200 linear response with the raw signal in the 50-100nA current range. The  $\phi_i$  in  
 201 equation (6) can be rewritten as:

$$\phi_i = a_i(A_i - A_{i-ped} + b_i), \quad (9)$$

202 where  $A_i$  and  $A_{i\_ped}$  are the recorded ADC value and pedestal value, and  $a_i$  and  
 203  $b_i$  are the slope and intercept of the relationship between  $\phi_i$  and  $A_i - A_{i\_ped}$ .  
 204 Equation (7) can be rewritten as:

$$D_U = \frac{(A_{U+} - A_{U+_{ped}} + b_{U+}) - h_u(A_{U-} - A_{U-_{ped}} + b_{U-})}{(A_{U+} - A_{U+_{ped}} + b_{U+}) + h_u(A_{U-} - A_{U-_{ped}} + b_{U-})}, \quad (10)$$

205 where  $h_u = a_{U-}/a_{U+}$ , and is related to the ratio of the signals for the  $U_+$  and  
 206  $U_-$  antennas and the gain settings of the two channels.

207 Combining the equation (9) and (4), the calibration constant  $b_i$  was obtained  
 208 by taking the linear fit between the ADC values of BPM and the beam current:  
 209  $I \propto (A_i - A_{i\_ped} + b_i)$ . Besides, the linear fit used a group of runs which had the  
 same beam position but different beam current Figure 11 shows the  $A_i - A_{i\_ped}$

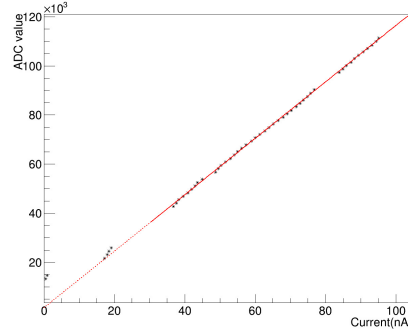


Figure 11: ADC value of BPM raw signal ( $A - A_{ped}$ ) V.S. current

210  
 211 versus the beam current. It can be seen that the ADC values were linear with  
 212 beam current in the considering current range of 50-100 nA. The intercept from  
 213 the linear fit of Fig.11 is the value  $b_i$ .

214 By transporting the position  $x_{harp}$  and  $y_{harp}$  in equation (2) from two harps  
 215 to the BPM local coordinate  $u_{harp}$  and  $v_{harp}$ , a fit between the BPM data  $U$   
 216 and the harp data  $U_{harp}$  determined three calibration constants  $c_0$ ,  $c_1$  and  $c_2$ :

$$U_{harp} = U_c = c_0 + c_1 u + c_2 v, \quad (11)$$

<sup>217</sup> where  $U_c$  is the calibrated BPM position. It was converted to Hall coordinate  $X_c$   
<sup>218</sup> for further transporting to the target location. An calibration example is shown  
in Fig. 12. The asterisks in Fig. 12 represent  $U_{harp}$ , and the dots represent  $U$ .

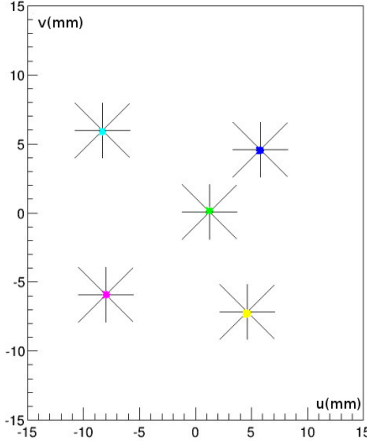


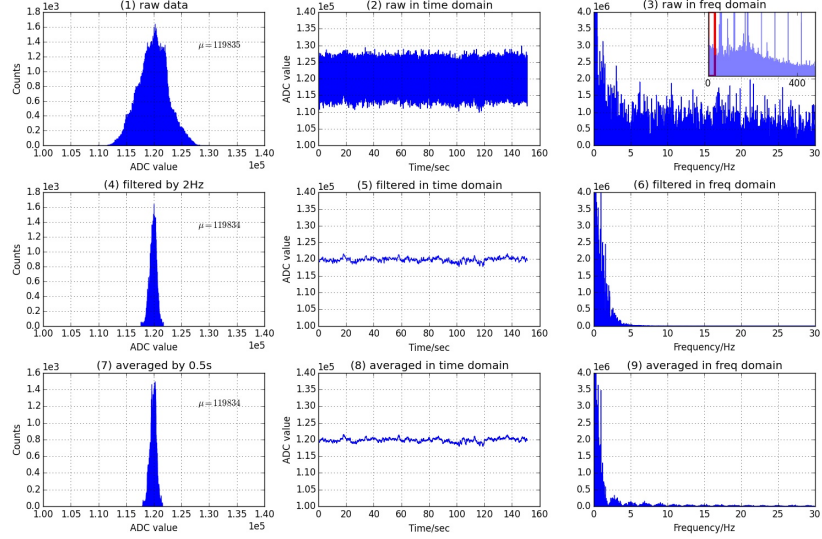
Figure 12: Harp scan data combined with BPM data, the asterisks are the positions from harp, while the dots are from BPM.

<sup>219</sup>

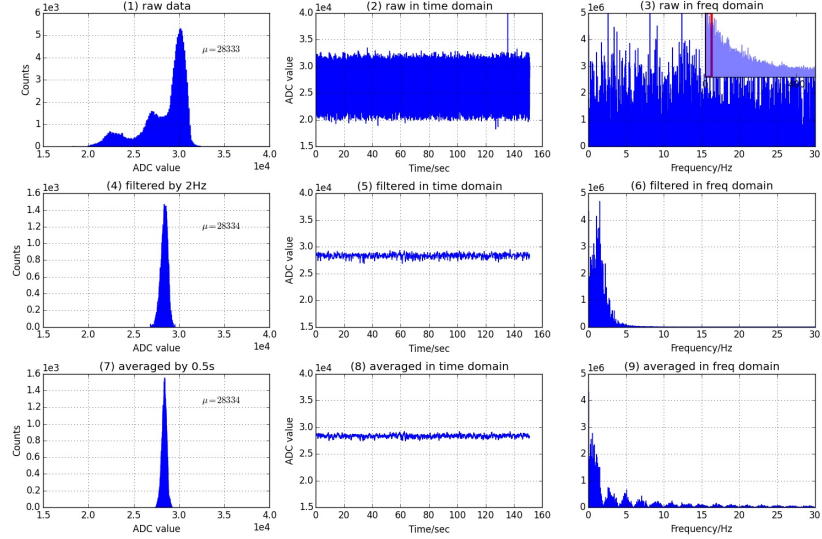
<sup>220</sup> In order to reduce the noise and improve the resolution during data analysis,  
<sup>221</sup> a software filter was applied. Since the 18 bit ADC was triggered by the helicity  
<sup>222</sup> signal with a fixed frequency, it could be regarded as a sampling ADC. Fig.13  
<sup>223</sup> shows the signal dealt with a 2 Hz low pass filter. The bottom 3 plots in Fig. 13  
<sup>224</sup> (a,b) are the averaged signal for comparing with the filtered signal. The average  
<sup>225</sup> procedure lead to the same result as the filter. The filter also erases the beam  
<sup>226</sup> displacement caused by the rasters, which is necessary to extract the position  
<sup>227</sup> of the beam center.

### <sup>228</sup> 3.3. Beam position reconstruction at the target

<sup>229</sup> It is easy to transport the position from the BPMs to the target by using a  
<sup>230</sup> linear transportation method for the straight through setting. For the settings  
<sup>231</sup> with a transverse magnetic field at the target, the linear transportation method  
<sup>232</sup> can not be used since the beam is bent near the target. A target magnet field  
<sup>233</sup> map [11] was generated from the TOSCA model. To test the accuracy of the



(a) Normal run with beam



(b) Pedestal run without beam

Figure 13: Software filter applied to BPM signal. (a) is the signal with beam, (b) is the pedestal signal without beam. (1,2,3) in (a,b) are the raw signal without applying the filter, (4,5,6) are applied a 2Hz finite-impulse-response filter with 4th order. (7,8,9) are averaged with 0.5 s. (1,4,7) are the signal's 1-D histogram, (2,5,8) are the signal in time domain, (3,6,9) are in frequency domain. Note all of the plots in (a) is for a single signal, same as in (b).

234 TOSCA model, the target magnet field was measured before the experiment  
 235 [12, 13]. The position and angle at target were calculated in terms of the  
 236 positions at BPMA and BPMB, together with the magnet field information.  
 237 Fits were used to speed up the calculation. To do this, a full simulation was  
 238 taken by generating thousands of trajectories with different initial positions and  
 239 angles. The fits were compared with the full simulation and they are consistent  
 with negligible difference. Fig. 14 shows the trajectories from the simulation.

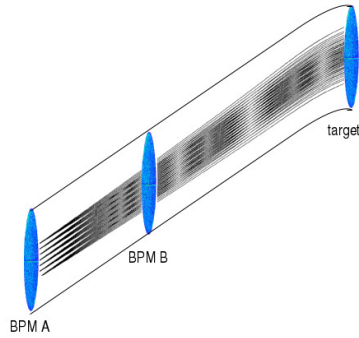


Figure 14: Transporting beam position from BPM to target with transverse target magnet field

240  
 241 The fitted transport functions were only used to transport the beam center  
 242 position from the two BPMs to the target by applying the 2 Hz filter, which  
 243 filtered out the fast raster and slow raster motion to keep only the beam center  
 244 position. The transported position were expressed as  $X_{center}$ .

245 *3.4. Determining the beam position event-by-event*

246 The readout of the magnet current for the two rasters was connected to  
 247 a series of ADCs. Two scintillator planes in the HRS form a DAQ trigger.  
 248 This pulse signal triggered the ADC to record the raster magnet current for  
 249 each event. The information from the rasters and the BPMs was combined  
 250 to provide the beam position event-by-event. The position at the target was  
 251 determined as:

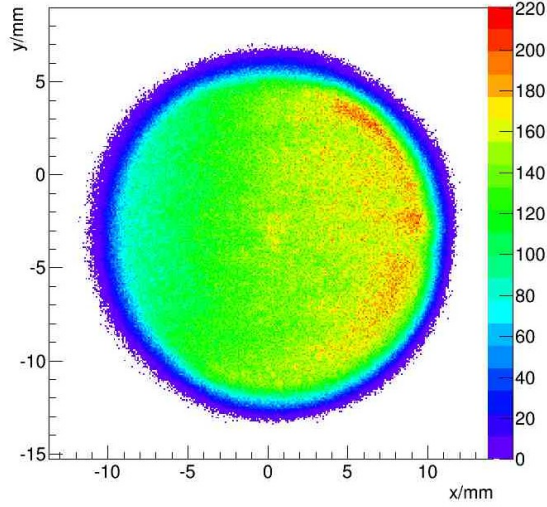


Figure 15: Reconstructed beam position at the target

$$X = X_{center} + X_{fstraster} + X_{slraster}, \quad (12)$$

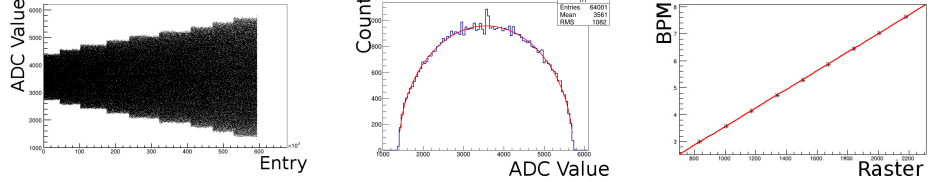
where  $X_{fstraster}$  and  $X_{slraster}$  were the position displaced by the fast raster and slow raster, respectively, which were converted from the current values of the two raster magnets. The calibration of the conversion factors between the magnet current of the rasters and the displaced position will be discussed in the next subsection. An example of reconstructed beam position is shown in Fig. 15.

#### 3.4.1. Conversion factor for the slow raster

Two methods were used to calibrate the conversion factor for the slow raster. The first method used the calibrated BPM information, i.e., comparing the raster magnet current with the beam shape shown in the ADC of the BPMs. Several calibrations were taken during different run periods at a beam current of 100nA using different values of the raster magnet current, as shown in Fig.16(a).

264

The range of the beam distribution at the target was calculated from the



(a) ADC value of slow raster, with the raster current changing

(b) Elliptical fit for the spread of magnet current of slow raster

(c) Linear fit between the raster current and the range of beam distribution

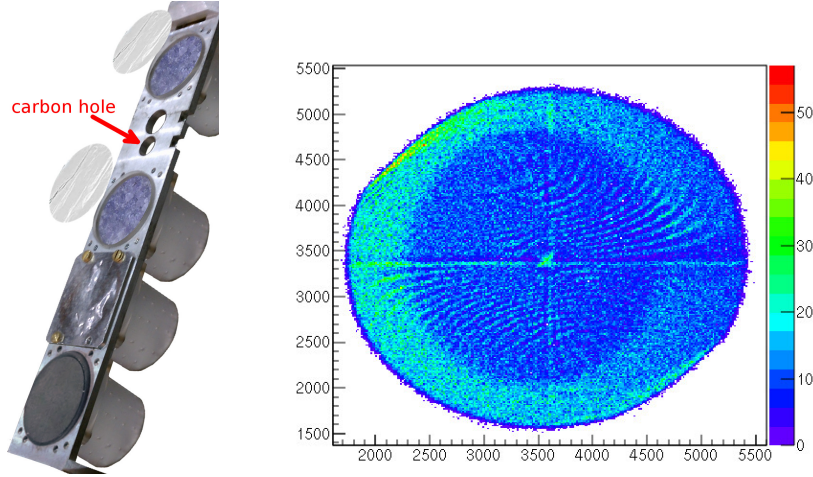
Figure 16: Converting the raster current to beam position shift

ranges at the two BPMs without applying the filter, using the transport functions fitted previously. The range of the beam distribution at the two BPMs and the amplitude of the raster current was calculated from an elliptical fit, an example is shown in Fig.16(b). Figure 16(c) shows a linear fit between the raster current and the range of the beam distribution at the target. The x axis in Fig.16(c) is the magnet current of the raster, and the y axis is the range of the beam distribution obtained from the BPMs.

The second method for calibrating the conversion factor used a target called “carbon hole” as shown in Fig.17(a).

Scattered electrons were used as the trigger for recording the raster magnet current. Since the density of the target frame was much higher than that of the “hole”, which was submerged in liquid helium, the density of events triggered from the target frame was much higher than that of the hole itself. Recorded values reveal a hole shape as shown in Fig.17(b). The size of the carbon hole was surveyed before the experiment, and a fit program was used to extract the radius of the recorded hole shape for that raster current. The conversion factor  $F$  was then calculated as the ratio of the size of the carbon hole  $S_{hole}$  and the radius of the hole shape  $R_{hole}$  in the ADC:

$$F = \frac{S_{hole}}{2 * R_{hole}}. \quad (13)$$



(a) Location for carbon hole target in target insert

(b) The shape of carbon hole in raster ADC, x and y axis are corresponding to the currents on x magnet and y magnet of slow raster, respectively.

Figure 17: Carbon hole method to calibrate raster

*3.4.2. Conversion factor for the fast raster*

The conversion for the fast raster was the same as for the slow raster. The low pass filter for the BPM was set to a higher value than the frequency of the fast raster to see the beam shape at the BPM formed by the fast raster. For a higher frequency filter, a larger beam current was needed to get a clear pattern. The beam current chosen for calibrating the fast raster was near 300 nA, which was the safety limit for the target. The beam shape formed by the fast raster is shown in Fig.18.

**4. Uncertainty**

The uncertainty of the final beam position at the target for each event contains several contributions:

- The first part comes from the uncertainty of the calibration constant. It includes the BPM resolution for the DAQ runs used for the calibration, the uncertainty of the harp data corresponding to each calibration, and

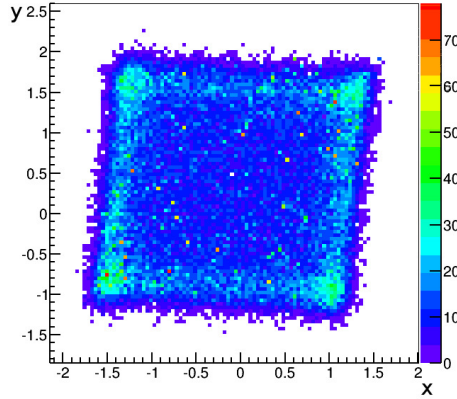


Figure 18: Beam shape formed by the fast raster at the BPM A location, the unit is millimeter

298       the survey uncertainties for the BPMs and harps. It contributes about 0.7  
 299       mm for the uncertainty of the position and 0.7 mrad for the uncertainty  
 300       of the angle.

301       • The uncertainty on the pedestal is the largest uncertainty for the beam  
 302       position measurement, contributing about 0.7~1.5 mm to the uncertainty  
 303       of the position and 0.7~1.5 mrad to the uncertainty of the angle.

304       • The uncertainties from the BPM survey need to be included, since the  
 305       production data and the calibration data were taken at different beamline  
 306       settings when the equipment was moved. They contribute 0.5 mm to the  
 307       uncertainty of the position.

308       • The uncertainty from the magnetic field map of the target was considered  
 309       for the settings with the target magnet field.

310       • The uncertainties due to the size conversion of the rasters were also in-  
 311       cluded.

312       The position uncertainty was magnified by a factor of 5 at the target because of  
 313       the short distance between the two BPMs. For example, in the straight through  
 314       setting, if the uncertainty at BPM A is 0.2 mm, and at BPM B is 0.27 mm,  
 315       the uncertainty at the target is 1.1 mm for position and 1.3 mrad for angle.

<sup>316</sup> The uncertainty for the position at the target was around 1~2 mm, while the  
<sup>317</sup> uncertainty for the angle was 1~2 mrad.

<sup>318</sup> **5. Summary**

<sup>319</sup> JLab g2p experiment used a transversely polarized  $NH_3$  target for the first  
<sup>320</sup> time in Hall A. It put a limit of below 100 nA on the electron beam current and  
<sup>321</sup> required a slow raster to spread beam to a large area. Two chicane magnets were  
<sup>322</sup> used to compensate the strong transverse magnetic field. Beam-line equipment,  
<sup>323</sup> including the BPMs, harps and associated readout system, were upgraded to  
<sup>324</sup> allow precision measurements of the beam position at low current (50-100 nA).  
<sup>325</sup> A software filter was used to reduce noise of the BPMs. A correction equation  
<sup>326</sup> was used to compensate the non-linearity caused by the diff/sum equation. The  
<sup>327</sup> harp data and the linear fit between the bpm signal and the beam current  
<sup>328</sup> were used to extract the calibration constant of the BPM. To account for the  
<sup>329</sup> strong target magnetic field effect, transport functions were fitted to transport  
<sup>330</sup> the beam position from the BPMs to the target. The beam position in the  
<sup>331</sup> x-y plane and the angle at the target location are extracted event-by-event by  
<sup>332</sup> combining information from the BPMs and the signals from the rasters. The  
<sup>333</sup> performance of the new devices (BPMs, harps and slow rasters) were presented  
<sup>334</sup> along with an analysis of systematic uncertainties.

<sup>335</sup> **Acknowledgments**

<sup>336</sup> This work was supported by DOE contract DE-AC05-84ER40150 under  
<sup>337</sup> which the Southeastern Universities Research Association (SURA) operates the  
<sup>338</sup> Thomas Jefferson National Accelerator Facility, and by the National Natural  
<sup>339</sup> Science Foundation of China (11135002, 11275083), the Natural Science Foun-  
<sup>340</sup> dation of Anhui Education Committee (KJ2012B179).

<sup>341</sup> **Reference**

- 342 [1] A. Camsonne, J. P. Chen, D. Crabb and K. Slifer, spokesperson, JLab  
343 E08-027 (g2p) experiment. 1
- 344 [2] D. G. Crabb, W. Meyer, Solid polarized targets for nuclear and particle  
345 physics experiments, Annu. Rev. Nucl. Part. Sci. 47 (1997) 67–109. 1
- 346 [3] R. Michaels, Precision Integrating HAPPEX ADC, JLab Technical report  
347 (unpublished).
- 348 URL [http://hallaweb.jlab.org/parity/prex/adc18/prex\\_adc18\\_](http://hallaweb.jlab.org/parity/prex/adc18/prex_adc18_spec.ps)  
349 [spec.ps](http://hallaweb.jlab.org/parity/prex/adc18_spec.ps) 2.1
- 350 [4] J. Musson, Functional Description of Algorithms Used in Digital Receivers,  
351 JLab Technical report No. JLAB-TN-14-028. 2.1
- 352 [5] C. Yan and et al., Superharp - A wire scanner with absolute position read-  
353 out for beam energy measurement at CEBAF, Nuclear Instruments and  
354 Methods in Physics Research A 365 (1995) 261–267. 2.2, 3.1
- 355 [6] J. Pierce, J. Maxwell, T. Badman, J. Brock, C. Carlin, D. Crabb, D. Day,  
356 C. Keith, N. Kvaltine, D. Meekins, J. Mulholland, J. Shields, K. Slifer,  
357 Dynamically polarized target for the and experiments at jefferson lab,  
358 Nuclear Instruments and Methods in Physics Research Section A: Acceler-  
359 ators, Spectrometers, Detectors and Associated Equipment 738 (0) (2014)  
360 54 – 60. doi:<http://dx.doi.org/10.1016/j.nima.2013.12.016>.  
361 URL [http://www.sciencedirect.com/science/article/pii/](http://www.sciencedirect.com/science/article/pii/S0168900213016999)  
362 [S0168900213016999](http://www.sciencedirect.com/science/article/pii/S0168900213016999) 2.3
- 363 [7] C. Yan, Hall C Polarized Target Raster System Upgrade, JLab Technical  
364 report (unpublished).  
365 URL [https://www.jlab.org/Hall-C/talks/01\\_06\\_05/yan.pdf](https://www.jlab.org/Hall-C/talks/01_06_05/yan.pdf) 2.3
- 366 [8] W. . Barry, A general analysis of thin wire pickups for high frequency beam  
367 position monitors, Nuclear Instruments and Methods in Physics Research  
368 A 301 (1991) 407–416. 3.2

- 369 [9] C.R.Carman, J. L. Pellegrin, The beam positions of the spear storage ring,  
370 SLAC-PUB-1227. 3.2
- 371 [10] P.Poit, Evaluation and correction of nonlinear effects in fnpl beam position  
372 monitors, FNPL Technical report No.Beams-doc-1894-v1.  
373 URL <http://beamdocs.fnal.gov/AD-public/DocDB>ShowDocument?docid=1894> 3.2
- 375 [11] R. Wines, private communication. 3.3
- 376 [12] J. Liu, Magnetic field mapping on a translation table, JLab Technical  
377 report, E08-027 Collaboration (unpublished).  
378 URL [http://hallaweb.jlab.org/experiment/g2p/collaborators/jie/2011\\_10\\_05\\_fieldmap\\_report/Target\\_Field\\_Report.pdf](http://hallaweb.jlab.org/experiment/g2p/collaborators/jie/2011_10_05_fieldmap_report/Target_Field_Report.pdf) 3.3
- 380 [13] C. Gu, Target field mapping and uncertainty estimation, JLab Technical  
381 report, E08-027 Collaboration (unpublished).  
382 URL [https://hallaweb.jlab.org/experiment/g2p/collaborators/chao/technotes/Chao\\_TechNote\\_TargetField.pdf](https://hallaweb.jlab.org/experiment/g2p/collaborators/chao/technotes/Chao_TechNote_TargetField.pdf) 3.3